energies

MDPI

Article

Fault Identification and Classification of Asynchronous Motor Drive Using Optimization Approach with Improved Reliability

Gopu Venugopal [1], Arun Kumar Udayakumar [2], Adhavan Balashanmugham [3], Mohamad Abou Houran [4], Faisal Alsaif [5], Rajvikram Madurai Elavarasan [6], Kannadasan Raju [7] and Mohammed H. Alsharif [8,*]

1 Department of Electrical and Electronics Engineering, Sri Ramakrishna Engineering College, Coimbatore 641022, Tamil Nadu, India
2 Department of Electrical and Electronics Engineering, SRM Institute of Science and Technology, Ramapuram Campus, Chennai 600089, Tamil Nadu, India
3 Department of Electrical and Electronics Engineering, PSG Institute of Technology and Applied Research, Coimbatore 641062, Tamil Nadu, India
4 School of Electrical Engineering, Xi'an Jiaotong University, Xi'an 710049, China
5 Department of Electrical Engineering, College of Engineering, King Saud University, Riyadh 11421, Saudi Arabia
6 Clean and Resilient Energy Systems (CARES) Laboratory, Texas A&M University, Galveston, TX 77553, USA
7 Department of Electrical and Electronics Engineering, Sri Venkateswara College of Engineering, Sriperumbudur, Chennai 602117, Tamil Nadu, India
8 Department of Electrical Engineering, College of Electronics and Information Engineering, Sejong University, Seoul 05006, Republic of Korea
* Correspondence: malsharif@sejong.ac.kr

Abstract: This article aims to provide a technique for identifying and categorizing interturn insulation problems in variable-speed motor drives by combining Salp Swarm Optimization (SSO) with Recurrent Neural Network (RNN). The goal of the proposed technique is to detect and classify Asynchronous Motor faults at their early stages, under both normal and abnormal operating conditions. The proposed technique uses a recurrent neural network in two phases to identify and label interturn insulation concerns, with the first phase being utilised to establish whether or not the motors are healthy. In the second step, it discovers and categorises potentially dangerous interturn errors. The SSO approach is used in the second phase of the recurrent neural network learning procedure, with the goal function of minimizing error in mind. The proposed CSSRN technique simplifies the system for detecting and categorizing the interturn insulation issue, resulting in increased system precision. In addition, the proposed model is implemented in the MATLAB/Simulink, where metrics such as accuracy, precision, recall, and specificity may be analysed. Similarly, existing methods such as Adaptive Neuro-Fuzzy Inference System (ANFIS), Recurrent Neural Network (RNN), and Salp Swarm Algorithm Artificial Neural Network (SSAANN) are utilised to evaluate metrics such as Root mean squared error (RMSE), Mean bias error (MBE), Mean absolute percentage error (MAPE), consumption, and execution time for comparative analysis.

Keywords: interturn short circuits (ITSC); Salp Swarm Optimization (SSO); recurrent neural network (RNN); Salp Swarm Algorithm Artificial Neural Network (SSAANN)

Citation: Venugopal, G.; Udayakumar, A.K.; Balashanmugham, A.; Houran, M.A.; Alsaif, F.; Elavarasan, R.M.; Raju, K.; Alsharif, M.H. Fault Identification and Classification of Asynchronous Motor Drive Using Optimization Approach with Improved Reliability. *Energies* **2023**, *16*, 2660. https://doi.org/10.3390/en16062660

Academic Editor: Lorand Szabo

Received: 21 February 2023
Revised: 8 March 2023
Accepted: 9 March 2023
Published: 12 March 2023

1. Introduction

Electric motors play a vital role in the reliable process of manufacturing facilities. The identification of motor anomalies will prevent costly breakdowns in manufacturing facilities. Bearing and stator-winding-related inadequacies account for around three-fourths of all failures in squirrel-cage motors, as deduced from [1–4]. Furthermore, it shows that turn-to-turn insulation failure is the primary cause of motor stator winding failures. Even though there is no trial data showing the time delay between the interturn and ground wall insulation failure phases, it is acceptable to presume that it does not occur instantaneously.

This is because there is a time difference between the two phases. In this method, the stator core and nearby coils may be safely removed from the motor if an interturn short is detected while the motor is running, reducing the need for repairs and the amount of time the motor is down for maintenance. Existing instrumentation can show the proximity of a shorted turn, but only while the motor is disabled. If these problems with the motors are not caught in time, the machinery will eventually break down [5]. When a machine fails, it may inflict harm on nearby workers. Downtime and unsuccessful machine repairs can incur significant costs. So, defect detection is crucial throughout the development phase [6]. Various conventional methods are available, each with its own set of advantages and disadvantages. For defect identification and diagnosis, mathematical models of the system are used. Bearing, stator, and eccentricity-related defects are briefly discussed in their diagnosis [7]. Methods for determining fault include Motor Current Signature Analyses (MCSA), axial flux-based techniques, and vibration analysis.

When insulation problems are modelled and tested, the machine draws unbalanced phase currents [8]. This imbalance creates a cascade of counter clockwise currents. Voltage imbalances and machine saturation cause negative sequence currents [9]. Time-frequency domain algorithms mentioned in the article include Singular Value Decomposition (SVD), Short-Time Fourier Transform (STFT), and Wavelet Transform (WT). Wavelet packet decomposition was used to identify the motor bearing fault conditions [10–12]. The aforementioned frequency-domain methods assume you already know or have a good approximation of the bearing failure frequencies. When the signal-to-noise ratio is low, it becomes more difficult to study the vibration spectrum, which is the second shortcoming. It is likely that the system will become more complicated if the vibration spectrum has many different frequency components [13–16]. An Artificial Neural Network (ANN) has the ability to grasp the problem of machine monitoring and failure discovery, utilizing an approach that is inexpensive, dependable, and does not need intrusive procedures [17–19]. On the other hand, although fuzzy logic is useful for making approximate inferences, it is not always able to provide precise accuracy [20].

In this study, we present a method for detecting and classifying interturn insulation faults in Asynchronous Motor (AM) adjustable motor drives by (CSSRN) combining Salp Swarm Optimization (SSO) with Recurrent Neural Network (RNN). The goal of the suggested method is to identify and categorise Asynchronous Motor (AM) symptoms at their earliest stages, both in normal and pathological contexts. The proposed system has the following contributions and advantages:

- Development of a simulation setup for the derivation of induction motor parameters under both healthy and faulty conditions
- Highly robust and efficient system that could facilitate an optimum solution for fault detection and condition monitoring of induction motor
- A comparative analysis with approaches such as ANFIS, RNN, and SSAANN is shown to prove the efficiency and reliability of the proposed system.

This paper's remaining sections are as follows. Recent research efforts and their historical context are discussed in Section 2. In Section 3, we see an example of the suggested approach for detecting and categorizing interturn faults in an Asynchronous Motor (AM). Interturn short circuits are shown in Section 4. In Section 5, we describe the suggested Recurrent Neural Network (RNN) that is based on Salp Swarm Optimization (SSO). The simulation results and analysis of the current and new methods are shown and discussed in Section 6.

2. Recent Research Works: A Brief Overview

Earlier studies on Asynchronous machine fault diagnosis have mostly concentrated on the identification of interturn errors in the Asynchronous Motor (AM) from a number of different angles and methods. The negative sequence current of the faulty machine may be compensated for with the help of a method proposed by M. Bouzid et al. [21]. The study's goal was to improve the reliability and sensitivity of early stator problem identification in

the presence of a wide range of disturbances. By using a closed-loop control system and an inverter, E. Elbouchikhi et al. produced a method for detecting problems in Asynchronous Motor (AM) stators [22]. Unbalanced currents in the stators result from defects such as phase-to-phase and phase-to-ground. Symmetrical Components (SCs) analysis of the stator current was used as part of the diagnostic procedure. The fundamental frequency and three-phase phasors were assessed using Maximum-Likelihood Estimation (MLE). Unbalance faults were identified using the Generalised Likelihood Ratio Test (GLRT). L. Maraaba et al. introduced Neural Networks (NNs) for analysing three phase Asynchronous Motor (AM) stator shorted turns [23]. The motor's output of electromechanical torque served as a fault indication. During the Neural Networks (NNs) training phase, we referred to the five individual motors as observed motors.

P. Rebouças Filho et al. [24] made a significant contribution to the field of Asynchronous generators by developing an effective approach for detecting impending stator winding interturn short-circuits in wind turbines. The generator may be put through a variety of short circuits on a wind turbine test bed. The electricity was purchased for a defect database. G. Surya et al. presented the ideal parameters for radial flux sensing stator flaw detection [25]. Flux signature analysis in comparison to traditional Motor Current Signature Analyses (MCSA) has been the focus of many prior research efforts. Two such difficulties, a turn fault and a cooling system failure, have been suggested and solved [26]. Regardless of whatever way it goes, the stator will become hotter. To solve this problem, researchers devised a thermal data analysis method based on two thermal profile indicators. Indicators such as this would be useful for diagnosing problems such as cooling system failure and faults in the interturn connections. D. Dorrell et al. [27,28] analysed the future impact of interturn faults. An evaluation of the rise in the proportion of current flowing in reverse was performed under both normal and abnormal operating circumstances for an Asynchronous Motor (AM). Simple algorithms were used for monitoring and fault identification, with the negative sequence component being a key factor in identifying interturn problems.

2.1. Background of the Research Work

Analysing previous studies shows that finding flaws at their earliest stages, such as Interturn Insulation Fault (ITIF) in the Asynchronous Motor (AM), is essential. Large amounts of electrical drives are installed in a factory. Therefore, in such a framework, identifying the state of each motor's health is crucial. Fault diagnosis is essential for preventing irreparable damage from occurring, as in the case of the unexpected breakdown of electric motor systems. Thus, correct motor modelling is the first step in the detection of motor anomalies. A variety of defect detection methods, including Neural Networks (NNs), Generalised Likelihood Ratio Test (GLRT), Fast Fourier Transform (FFT), etc., have been developed in light of the text. Artificial Neural Network (ANN) is capable of tackling the issue of motor monitoring and fault identification, despite the fact that it does not give heuristic reasoning during the fault detection process [29,30]. However, when applied to real-world problems, the most serious drawbacks of Artificial Intelligent systems are their inaccessible data processing structures and high computing costs. Additionally, because various states have varied needs, the initial training stage might be difficult due to the necessity for a vast library of stator currents. For optimal performance, this stage is crucial, although it may only allow for a limited setup of systems. However, it is not always feasible to predict the frequencies of bearing failure in advance, which is a drawback of FFT analysis and other frequency-domain approaches. There is also a problem when the signal-to-noise ratio is too high or too low; in these circumstances, the vibration spectrum has an excessively high number of components. The aforementioned techniques are used to predict the interturn errors; however, the complexity of the algorithm is high due to the large number of samples required. To avoid these challenges, cutting-edge technology must be used for defect detection and categorization at its best. Few control strategies are shown

to detect and categorise interturn faults in earlier studies; these limitations motivated us to conduct this study.

2.2. Fault Detection Approaches

Errors may occur everywhere, including the stator, rotor, bearings, and external peripherals of an Asynchronous Motor or Machine. Figure 1 presents examples of the several methods that may be used to spot Asynchronous Motor faults. Model-based methods, signal-processing-based methods, and AI-based methods are the three major groups into which the methods fall.

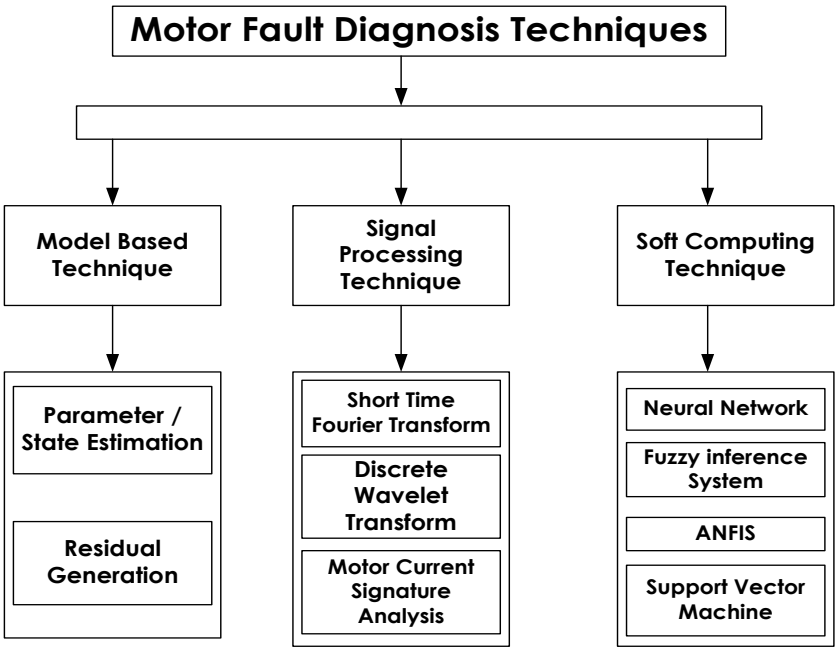

Figure 1. Various fault detection approaches for Asynchronous Motor.

The use of mathematical models of the system is at the heart of model-based approaches. However, it is challenging to construct a mathematical model that accurately represents a physical system. It is not possible to accurately predict defects and noises, and system characteristics may change over time. Thus, even in fault-free operation, the real system (the motor) never quite matches up with the model. These discrepancies are problematic because they may lead to false alarms or missed alerts in condition monitoring and fault detection applications.

Researchers have made several reports of their efforts to use AI in motor monitoring and defect detection. In this context, expert systems have been frequently used as a method of finding problems. Artificial Neural Networks (ANNs), Fuzzy Logic (FLs), and Support Vector Machines (SVMs) are just some of the AI methods that have been created and put to use in defect monitoring. Expert systems are often taught with the use of a database that links measurements to their associated errors. While the training database may include uniformly spaced defects of a certain severity, this may not be the case in real-world applications. This may cause incorrect diagnoses. In order to create an intelligent motor fault detection system, vibration signals from faulty induction motors were analysed using an extension neural network (ENN) [31]. The RNN method, which involves stacking two LSM layers to build a single end-to-end network, is widely used for analysing real-time safety monitoring in induction motors [32,33].

Recent advancements in Digital Signal Processing have made it possible to conduct real-time motor problem diagnostics using just a few signals (such as stator line current or vibration signals) acquired from the motor. This makes it easier to find motor problems and save money. DSP is used to rapidly analyse the current measurement for both the

fundamental component and the fault signature frequency, and the fault code is integrated into the algorithm. Several digital signal processing (Fast Fourier Transform (FFT) and Discrete Wavelet Transform (DWT)) approaches based on-line fault detection strategies were developed for Asynchronous Motors, taking into consideration the reliability and improved efficiency of digital processing techniques.

3. Proposed Method for Fault Detection in Asynchronous Motor (AM) Drive

The suggested approach to detect and classify an interturn defect in the Asynchronous Motor (AM) is shown in Figure 2. The suggested architecture's system is meant to monitor the system's condition while measuring a wide range of electrical parameters. In this case, the suggested process is split into two phases. Some examples are Asynchronous Motor (AM) fault detection and categorization and interturn fault detection. First, we use the Salp Swarm Optimization (SSO) method to determine if the motors are in good working order. Second, the Recurrent Neural Network (RNN) acts out the categorization of motors in poor health to identify the appropriate interturn faults for safety. The suggested detection and classification approach was created with the specific intended purpose of separating the Asynchronous Motor (AM) state from fault problems.

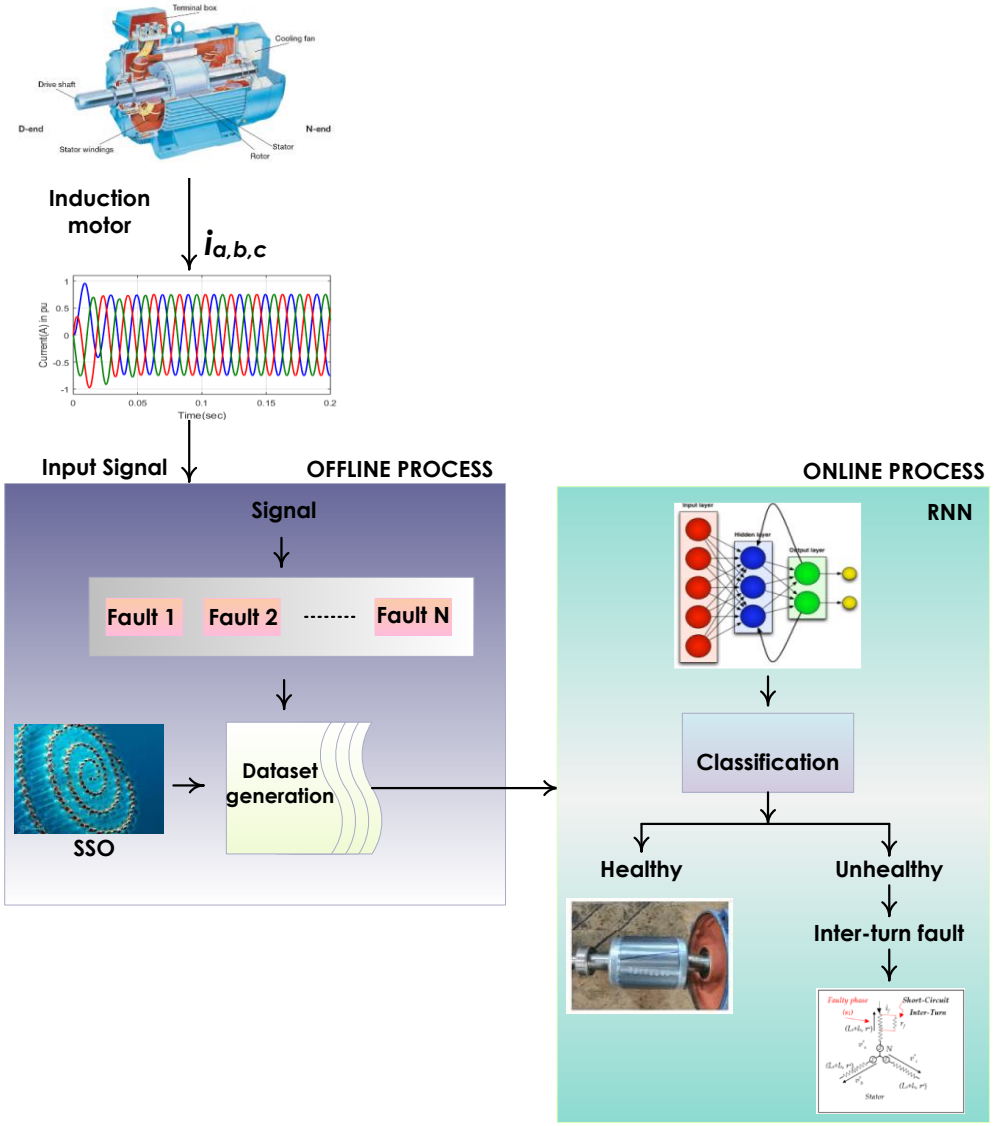

Figure 2. Flow of Proposed Block Diagram.

3.1. General Considerations of Interturn Short Circuits

This section describes a foundational understanding of interturn short circuits. In Figure 3, we see a single-phase coil winding with a short circuit between the turns. The following equation describes the sequence of magnetic field (MMF) waves generated by the stator winding of a symmetric Asynchronous Motor.

$$f_s(t,\theta) = \sum_{\mu} f_\mu \cos\left[\sigma_1 t - \mu p\theta\right] \tag{1}$$

Here, the number of pole pairs is denoted as p, mains angular frequency is indicated as σ_1 and $\mu = 6g + 1$, where $g = 0, \pm1, \pm2, \ldots$.

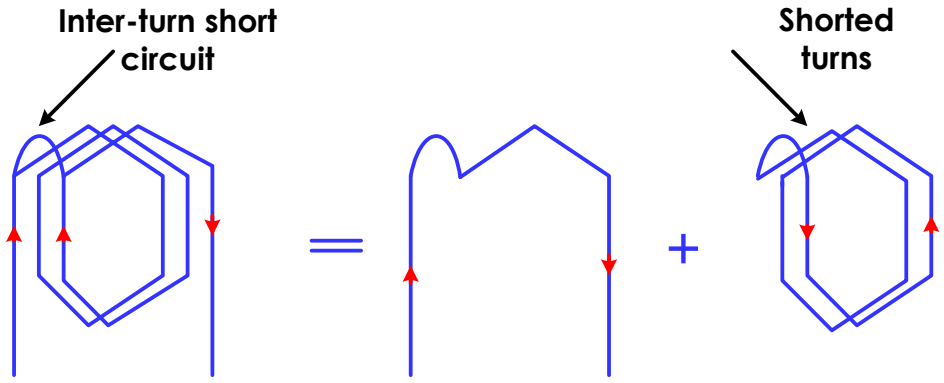

Figure 3. Representation of Interturn Fault in Single Phase Winding.

The rotor winding MMF may be calculated using the Fourier series. By ignoring the slot width opening $\alpha = 0$ and substituting $\alpha_i = 2\pi/n$ and $\sigma_i = 1$, it is easy to display that the MMF is produced by the base frequency I_r with amplitude $i_{rotor,\,max}$ that flow in a single rotor loop.

$$f_{loop,1}(t,\theta_{rotor}) = \sum_{c=1}^{\infty} \left[k_c \cos(c\theta_{rotor} + s\sigma_1 t) + k_c \cos(c\theta_{rotor} - s\sigma_1 t)\right] \tag{2}$$

where,

$$k_c = \frac{2}{c\pi}\left(1 - \frac{1}{y}\right) \sin\left(c\frac{\pi}{y}\right) i_{rotor,\max} \tag{3}$$

In the rotor, the neighbouring loop is shifted by $2\pi/y$ rad in space, the same amplitude and frequency of the current is phase shifted by $p \times (2\pi/y)$.

$$f_{loop,2}(t,\theta_{rotor}) = \sum_{c=1}^{\infty}\left[k_c \cos\left(c\theta_{rotor} + s\sigma_1 t - (c+p)\frac{2\pi}{y}\right) + k_c \cos\left(c\theta_{rotor} - s\sigma_1 t - (c-p)\frac{2\pi}{y}\right)\right] \tag{4}$$

When all the rotor loops' MMFs are added together, we can obtain the following equation for the overall rotor MMF:

$$f_{rotor}(t,\theta_{rotor}) = \sum_{i=0}^{y-1}\sum_{c=1}^{\infty}\left[k_c \cos\left(\begin{array}{l} c\theta_{rotor} + s\sigma_1 t - i\times \\ (c+p)\frac{2\pi}{y} \end{array}\right) + k_c \cos\left(\begin{array}{l} c\theta_{rotor} - s\sigma_1 t - i\times \\ (c-p)\frac{2\pi}{y} \end{array}\right)\right] \tag{5}$$

For $c = p$, $c = \rho y \pm p$ MMF waves exist, then the "c" can be $a + ve$ integer. Because $c = p$ represents the armature's reaction on the stator side to the fundamental MMF harmonic, $\rho y \pm p$ denotes the order of the so-called rotor slot harmonics, which are distinct from the fundamental MMF harmonic. The MMF waves, when seen from the side of the stator, have the following equation:

$$f_{rotor}(t,\theta_{rotor}) = f_{rotor1}\cos\left[\left(1-\rho\frac{y}{p}(1-s)\right)\sigma_1 t + (\rho n - p)\theta + f_{rotor2}\cos\left(1+\rho\frac{y}{p}(1-s)\right)\sigma_1 t - (\rho n - p)\theta\right] \quad (6)$$

It has been shown that higher-frequency rotor currents cause greater harmonic flux density waves from the side of the stator, which in turn cause MMF waves with a similar structure since the MMF waves are of the same frequency but have a varying number of pole pairs.

$$f_{rotor\mu}(t,\theta) = f_{rotor\mu 1}\cos\left[\left(1-\rho\frac{y}{p}(1-s)\right)\sigma_1 t + (\rho n - \mu p)\theta + f_{rotor2}\cos\left(1+\rho\frac{y}{p}(1-s)\right)\sigma_1 t - (\rho n - \mu p)\theta\right] \quad (7)$$

The flux density of a wave of a certain form may be obtained by multiplying MMF waves with an air-gap of constant permeance. Flux-density waves in the stator windings might set off electromagnetic fields and, in turn, current flow. Other EMFs can only be detected at the rotor slot frequency, in addition to the EMF at the base frequency. The MMF waves in Equation (20) become significant when the number of pole pairs of flux-density waves approaches a critical value (21). As long as the number of pole pairs remains the same as the original winding, the most essential frequency components will be present. Flux-density wave variations may be well explained by considering the air-gap permeance function of the slots in the stator and rotor. A stream of waves with a fixed frequency is produced. The stator current spectra reflect all waves with flux-density from the rotor side under the following situation due to the rotor cage winding nature:

$$(1 \pm \rho n(1-s)/p)a_1, \rho = 1, 2, \cdots$$

Under interturn short circuit circumstances, a new sequence of MMF waves emerges, for which the equations are as follows.

$$f_{add}(t,\theta) = \sum_{\substack{q=-\infty \\ q\neq 0}}^{\infty} f_{add}\cos(\alpha_1 t - q\theta) \quad (8)$$

Therefore, the positive and negative poles as well as both axes of rotation have magnetic fields (MMF) and a flux-density of waves. Although the flux-density wave in the apparatus spins in the opposite direction from each of these waves, each has the same number of pole pairs. Due to the wave's Asynchronous of just the base frequency component, it has no impact on the stator current spectrum. Currents can only be generated by rotor slot harmonic frequencies and electromagnetic fields (EMFs). Only an increase in the harmonic frequencies (rotor slot) is to be expected since a problem with the stator windings does not result in the emergence of a new frequency component in the stator current spectrum. There are two basic reasons why harmonic frequencies could be expected. When there is a malfunction, the machine experiences a greater number of flux-density waves, all of which have the same frequencies. Second, the wave with the present set of poles is one with a larger flux density.

3.2. Illustration of Interturn Short Circuit

This section presents an illustration of interturn short circuit. In the first case, the coil has just one turn. There is a short circuit between turns a and b, as shown in Figure 4. It is assumed that a short circuit forms between places a and b in the interturn and the associated issues are shown.

Looking closely at the diagram, it can be seen that the channel used by the circulating current is completely closed. The M-N route may be extended in two separate circuits, as predicted by the elementary theory. Phase current and SCC are two currents that generate MMFs in the opposite direction. Therefore, there is a localised area around the shorted turn(s) where the MMF is reduced due to the cumulative impact of interturn short circuits.

Because the phase winding has fewer turns when a SC occurs, the MMF is diminished. Additionally, the direction of the short-circuit current's MMF is counter to that of the phase winding's MMF. Longer shorts between turns may be analysed in the same manner. Slots and end winding regions are standard features on commercially available Asynchronous Motors (AMs), serving to separate coils. That is why you will often see interturn between coils that have identical turn counts. As such, we anticipate the occurrence of both interturn short circuits between adjacent turns in the same coil and half-coil short circuits. This is the equivalent of a phase that is 8% of a turn short. A mutual magnetic field (MMF) is generated whenever a short circuit occurs between two consecutive turns due to the mutual inductance between the phase winding and the other circuits in the machine. In addition, the additional phase of short-circuiting known as "phase D" is included. This phase is electrically isolated from the other phases yet linked to all other circuits on the rotor and stator sides. It is implicit once again that the rotor loop currents and the currents in the stator circuit are independent. The link between the rotor loop currents is subsequently formed using a matrix of rotor parameter r_{rotor} and $l_{rotor,rotor}$. The link between the stator windings is what determines the nature of the interaction that exists between the stator currents.

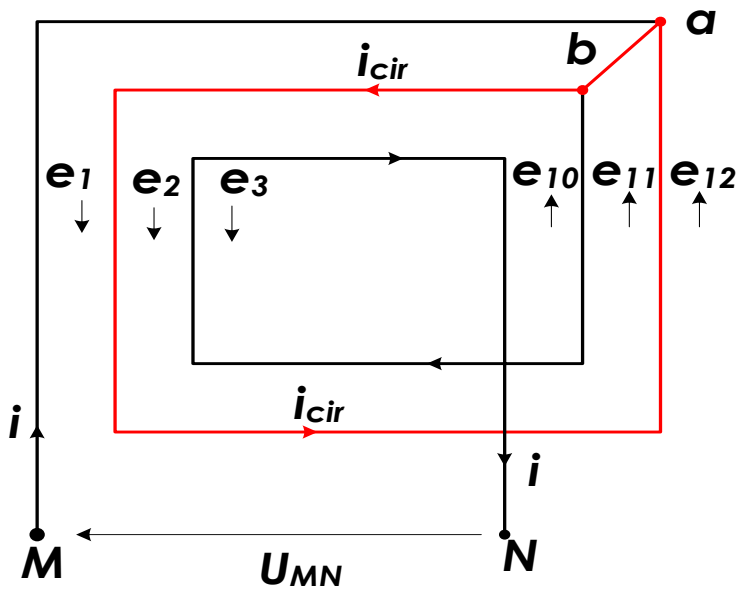

Figure 4. Interturn short circuit between points a and b.

3.3. Illustration of Star Connected Stator Windings during Interturn Short Circuit

Figure 5 illustrates the stator star winding configuration that happens during aninterturn short circuit. Whenever the stator windings and the voltage supply are mirror images of one another, there is no modification to the preceding equation. Some adjustments must be made to the stator currents and the simulation model so that line-to-line voltages may be used as inputs in the unbalanced connections or an unbalanced supply scenario to fulfil the KCL rule [34,35]. When this situation arises, a modification is made to Equation (1), as shown below:

$$\begin{bmatrix} a_{sa} \\ a_{sb} \\ a_{sc} \\ 0 \end{bmatrix} = \begin{bmatrix} r_a & -r_b & 0 & 0 \\ 0 & r_b & -r_c & r_a \\ -r_a & 0 & r_c & 0 \\ 0 & 0 & 0 & r_d \end{bmatrix} \begin{bmatrix} i_a \\ i_b \\ i_c \\ i_d \end{bmatrix} + \frac{d}{dt} \begin{bmatrix} \chi_{sa} \\ \chi_{sb} \\ \chi_{sc} \\ \chi_{sd} \end{bmatrix} \quad (9)$$

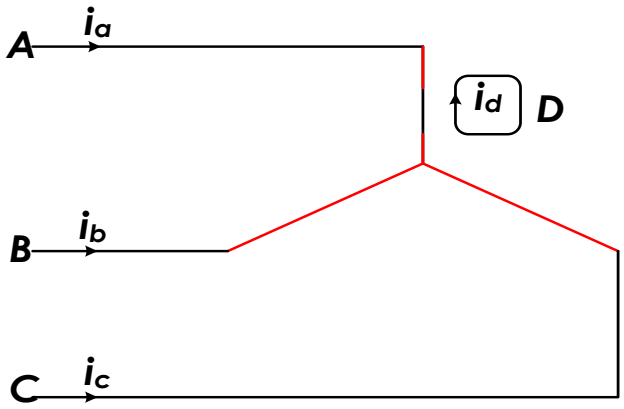

Figure 5. Interturn short circuit in Star Connected Stator winding.

Here, stator L-L voltages are u_{si}, $i = a, b, c$, the stator voltages vector zero term indicates the short-circuited phase.

$$\begin{bmatrix} \chi_{sa} \\ \chi_{sb} \\ \chi_{sc} \\ \chi_{sd} \end{bmatrix} = \begin{bmatrix} l_{aa} & l_{ab} & l_{ac} & l_{ad} \\ l_{ba} & l_{bb} & l_{bc} & l_{bd} \\ l_{ca} & l_{cb} & l_{cc} & l_{cd} \\ l_{da} & l_{db} & l_{dc} & l_{dd} \end{bmatrix} \begin{bmatrix} i_a \\ i_b \\ i_c \\ i_d \end{bmatrix} + \frac{d}{dt} \begin{bmatrix} l_{a,r} \\ l_{b,r} \\ l_{c,r} \\ l_{d,r} \end{bmatrix} \tag{10}$$

$$\begin{bmatrix} \chi_{sa} \\ \chi_{sb} \\ \chi_{sc} \\ \chi_{sd} \end{bmatrix} = \begin{bmatrix} l_{aa} & l_{ab} & l_{ac} & l_{ad} \\ l_{ba} & l_{bb} & l_{bc} & l_{bd} \\ 1 & 1 & 1 & 1 \\ l_{da} & l_{db} & l_{dc} & l_{dd} \end{bmatrix} \begin{bmatrix} i_a \\ i_b \\ i_c \\ i_d \end{bmatrix} + \frac{d}{dt} \begin{bmatrix} l_{a,r} \\ l_{b,r} \\ 0 \\ l_{d,r} \end{bmatrix} [i_r] \tag{11}$$

3.4. Illustration of Delta Connected Stator Windings during Interturn Short Circuit

Shorting between turns in a phase winding at terminals A and B is seen in Figure 6. If the stator's windings are linked in a delta configuration, no alterations need to be made to the equation system. The phase voltages, or line-to-line voltages, are used as an input to the model. Under asymmetrical circumstances in delta-connected windings, the line currents add up to zero, but the phase currents do not.

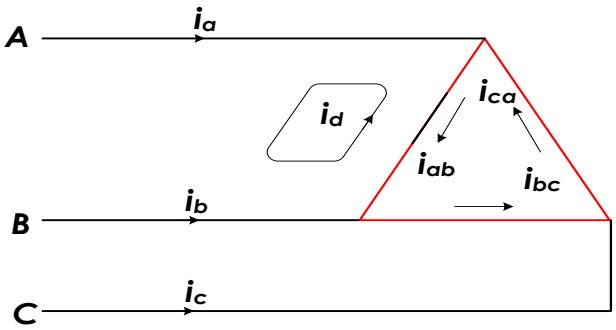

Figure 6. Interturn short circuit in Delta Connected Stator winding.

4. Proposed Salp Swarm Optimization (SSO) Based Recurrent Neural Network (RNN)

The proposed approach employs RNN in two independent steps, with the ultimate aim being the prediction and classification of healthy and unwell circumstances in Asynchronous Motor (AM). In this case, the RNN's second-stage learning is enhanced by applying the SSO method to the least-error goal function. The SSO method was introduced by S. Mirjalili [28] in 2017 as a novel approach to resolving the single- and multi-objective optimization issue. The swarming behaviour of crabs while navigating and feeding in water served as the primary idea for SSO. The SSO's self-adjusting mechanism keeps it

from settling into a minimal state (or maximum). In the end, SSO produces optimal or near-optimal solutions when the optimization process is complete. During the early stages of the optimization process, the SSO investigates the search space before transitioning to the latter phase of exploiting it. The proposed method evaluates the system's security and classifies the Asynchronous Motor (AM) interturn failure.

4.1. Optimization Steps

Step 1: Initialization

The speed, voltage, and torque values serve as the initialization parameters for the system constraint, while the power values serve as the initialization parameters for the RNN. The starting points for the salps' locations are written as,

$$Init_i = Random * (up_i - low_i) + low_i \;\; i = 1, 2, \ldots\ldots m \tag{12}$$

Step 2: Random Generation

The initialised power value with respect to time is generated at random after initialisation, and the equation is as follows:

$$p_{random}(t) = \begin{bmatrix} p_{11}(t) & p_{12}(t) & \cdots & p_{1n}(t) \\ p_{21}(t) & p_{22}(t) & \cdots & p_{2n}(t) \\ \vdots & \vdots & \vdots & \vdots \\ p_{m1}(t) & p_{m2}(t) & \cdots & p_{mn}(t) \end{bmatrix} \tag{13}$$

Here, p_{random} (t) is used to indicate the random creation of power with regard to time during the occurrence of the fault.

Step 3: Evaluation

During the assessment phase, the voltage and current levels that are in accordance with the produced power values will be revealed. The goal function of the suggested technique is assessed to ensure the smallest possible discrepancy between the desired and actual power signal. The objective function $of_i(t)$ is given by,

$$of_i(t) = \min\left\{o^{trg}(t) - o(t)\right\} \tag{14}$$

$$Subject \;\; to \begin{cases} v_{abci}^{\min}(t) \le v_{abci}(t) \le v_{abci}^{\max}(t) \\ N^{\min}(t) \le N(t) \le N^{\max}(t) \\ \tau^{\min}(t) \le \tau(t) \le \tau^{\max}(t) \end{cases} \tag{15}$$

where the actual and target power signal of the Asynchronous Motor (AM) is indicated as $o^{trg}(t)$ and $o(t)$. The system's defect should not be anticipated while its restrictions are within the range of limit, where the target signal may be determined.

Step 4: Leader Position Updating

Depending on the following formula, the leader salps position is rationalised.

$$Leader\ position_i = \begin{cases} F_j + R_1\left[(up_j - low_j)R_2 + low_j\right] & R_3 < 0.5 \\ F_j - R_1\left[(up_j - low_j)R_2 + low_j\right] & else \end{cases} \tag{16}$$

Step 5: Investigation and operation

It is the initial random number of the SSO algorithm that ensures that the exploration and exploitation phases are in a stable equilibrium.

$$R_1 = 2 \cdot \exp\left[-\left(\frac{4n}{Iter_{\max}}\right)^2\right] \tag{17}$$

where current iteration is represented as n and maximum numbers of iterations are represented as $Iter_{max}$.

Step 6: Follower Position Updating

The current location of the salp is calculated using Newton's law of motion and shown as,

$$Follower_j^i = \frac{t}{2}(at + v_o) \quad \forall \geq 2 \tag{18}$$

The number of iterations used in the optimization process is a representation of time, with the difference between iterations set to 1. The aforementioned equation is then written as,

$$Follower_j^i = \frac{1}{2}\left(Follower_j^i - Follower_j^{i-1}\right) \quad \forall i \geq 2 \tag{19}$$

To pinpoint the specific error, the algorithm's output is represented as follows. Figure 7 presents a diagram of the suggested SSO algorithm's flow.

$$\begin{bmatrix} v_{11}i_{11}(t) & v_{12}i_{12}(t) & \cdots & v_{1n}i_{1n}(t) \\ v_{21}i_{21}(t) & v_{22}i_{22}(t) & \cdots & v_{2n}i_{2n}(t) \\ \vdots & \vdots & \vdots & \vdots \\ v_{m1}i_{m1}(t) & v_{m2}i_{m2}(t) & \cdots & v_{mn}i_{mn}(t) \end{bmatrix} = \begin{bmatrix} f_{11}(t) & f_{12}(t) & \cdots & f_{1n}(t) \\ f_{21}(t) & f_{22}(t) & \cdots & f_{2n}(t) \\ \vdots & \vdots & \vdots & \vdots \\ f_{m1}(t) & f_{m2}(t) & \cdots & f_{mn}(t) \end{bmatrix} \tag{20}$$

4.2. Detection of Optimal Parameter Using Recurrent Neural Network

Learning and perception are inherent to RNNs since RNNs are made up of a network of artificial neurons. Adjusting the weights and biases of the interlayer connections between the neurons is how it is learned. Layers of incoming data, hidden processing, and output data are essential to RNN function. Nodes representing normalised conditions retrieved from intentional errors are included in the input layer. The hidden layer and the output layer both used sigmoid activation algorithms. Binary levels of 'Healthy' (H) and 'Unhealthy' (U) conditions may be assigned to the objective assessments from the two nodes at the system's output. In this case, the RNN was designed, implemented, and tested using the MATLAB/Simulink environment.

Step 1: The input vector ω is applied to the input layer. The RNN input is the error $e_r(t)$ and the error deviation $DE_r(t)$. Then, the equation for the input vector is given by,

$$\omega = \{\omega_1, \omega_2, \omega_3 \cdots \omega_m\}^T \tag{21}$$

The jth hidden unit of the net input is given by,

$$Hid_j^h = \sum_{i=1}^{m} z_{ji}\omega_i + \sigma_j^h \tag{22}$$

Step 2: The output of the neurons in the hidden layer is outlined in the following way:

$$M_j^h = f\left(\sum_{i=1}^{m} z_{ji}\omega_i + \sigma_j^h\right) \tag{23}$$

With this change, the net input to the output layer neurons is,

$$Hid_k^o = \sum_{j=1}^{m_h} z_{ji}\omega_i + \sigma_j^o \tag{24}$$

Step 3: Finally, the yield of the neurons i.e., actual output of the feed forward loop P_{act} in the output layer, is,

$$O_k^o = f\left(\sum_{j=1}^{m_h} z_{ji}\omega_i + \sigma_j^o\right) \tag{25}$$

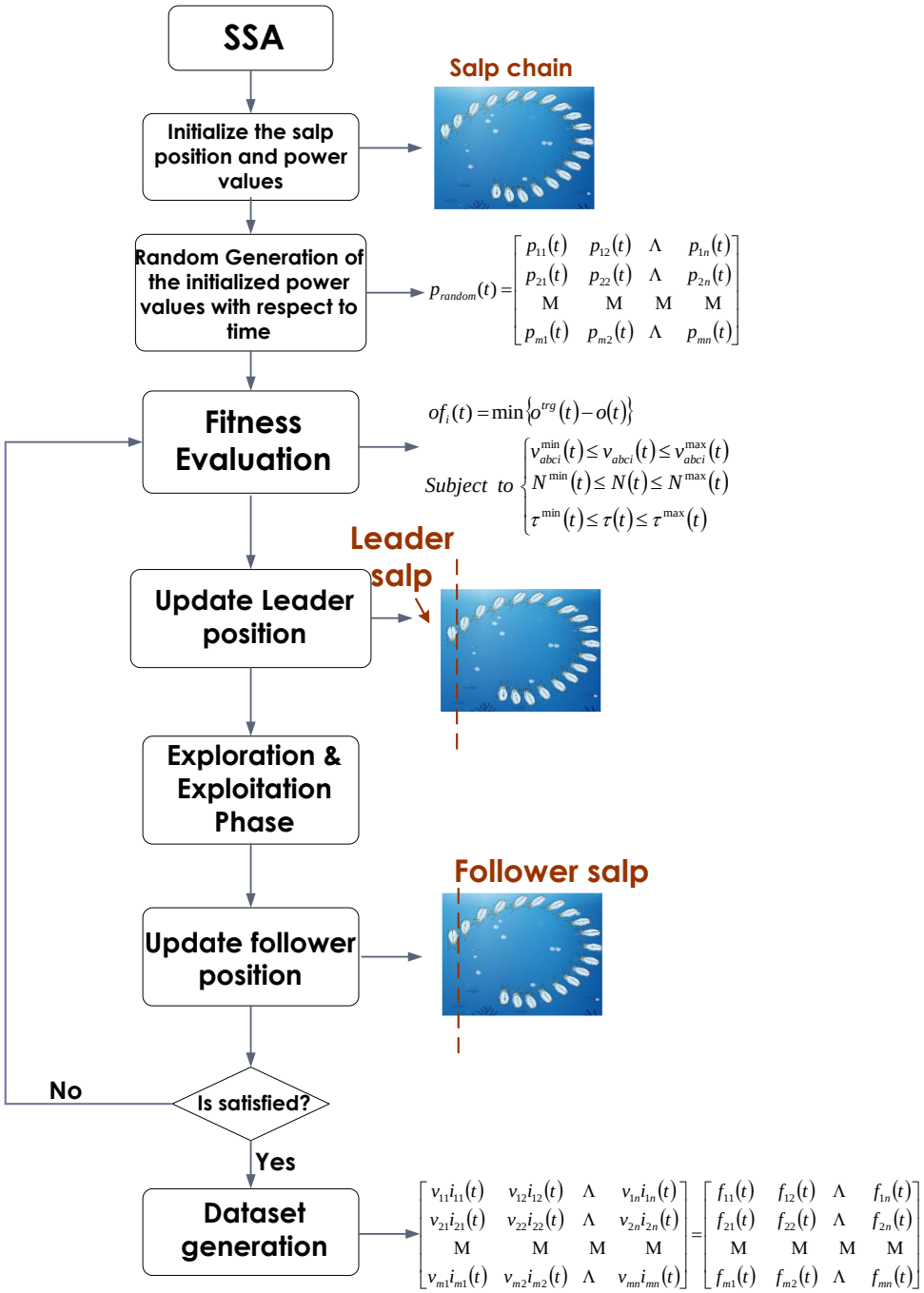

Figure 7. Flowchart of SSO algorithm.

Step 4: A gradient-descent strategy utilised by the back propagation algorithm is applied to the weights and biases in an attempt to minimise a Measurement System Analysis (MSA) performance index. The input of the RNN shown in Figure 8 is the error $e_r(t)$ and the deviation of error $DE_r(t)$, which is given as,

$$e_r(t) = v_o(t) - v_{ref}(t) \tag{26}$$

$$DE_r(t) = e_k(t) - e_{k-1}(t) \tag{27}$$

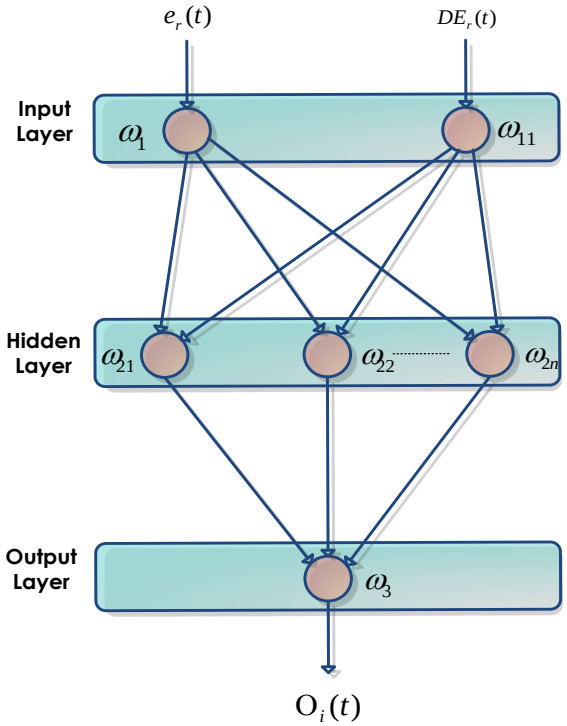

Figure 8. RNN Structure.

Step 5: The updating expressions and their corresponding synaptic weights are as follows.

$$z_{ji}(n+1) = z_{ji}(n) - \xi\left(\frac{\partial MSE}{\partial z_{ji}(n)}\right) + \beta\Delta z_{ji}(n) \tag{28}$$

$$\Delta z_{ji}(n) = z_{ji}(n) - z_{ji}(n-1) \tag{29}$$

5. Results and Discussion

The suggested method is realised and implemented in the MATLAB/Simulink platform. An intact IM may be distinguished from one that was damaged by the interturn fault using the proposed technique. The performance of the proposed control system is compared to that of the already-existing ANFIS, RNN, and SSAANN techniques. Performance metrics including RMSE, MAPE, MBE, and consumption time are examined in addition to standard measures of execution such as accuracy, recall, precision, and specificity. The following is an explanation of how the Asynchronous Motor (AM) works optimally. Table 1 shows the specifications of the Asynchronous Motor.

Table 1. Specifications of Asynchronous Motor.

Specification	Values
Induction Motor	3 Phase Squirrel Cage Induction Motor
Poles	4
Power Rating	1 HP
Voltage Rating	415 V
Operating Frequency	50 Hz
Current Rating	1.8 Amps

5.1. Simulation Results of Performance of Asynchronous Motor (AM) under Healthy Condition

The effectiveness of Asynchronous Motors (AMs) in a healthy state is investigated here. Stator current, d-axis voltage, q-axis voltage, and torque efficiency under normal

circumstances are shown in Figure 9. Figure 9 shows that there is no conflict between the fault events in the IM and the stator's operational parameters.

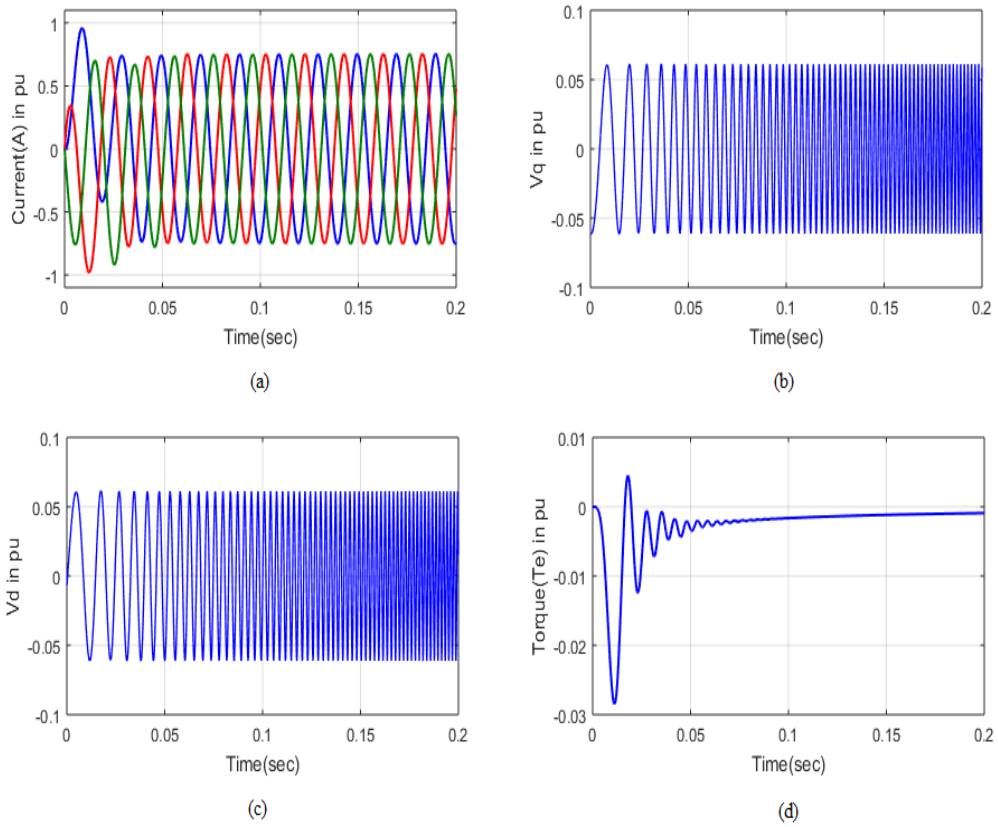

Figure 9. Output Waveforms (**a**) I_s (**b**) V_{sd} (**c**) V_{sq} (**d**) T_s.

5.2. Simulation Results of Performance of Asynchronous Motor (AM) under Unhealthy Condition

The effectiveness of the Asynchronous Motor (AM) in unfavourable circumstances is investigated here. The effectiveness of the Asynchronous Motor (AM) is examined in a healthy setting in Figure 10. Under Figure 9, we can see how I_s and V_s along the d-axis, stator voltage along the q-axis, and torque all fare in 10% unhealthy phase A circumstances. The current through the stator at 10% phase A shorted turns is shown in Figure 10a. The breakdown may be observed in time in Figure 10a, which is between 0.08 and 0.12 s.

Figure 10b displays the stator voltage along the d-axis when 10% of the turns are shorted in phase A. The defect in the stator voltage is shown in the figure to occur between 0.08 and 0.12 s after the fault has occurred, during which time the stator voltage is shown to be flowing normally. The q-axis stator voltage is shown in Figure 10c for 10% phase A shorted turns. As seen in Figure 10c, the stator voltage at the q axis was stable for the first few seconds until a problem emerged at t = 0.08 to 0.12 s. Ten percent of the torque applied in phase A during short turns is seen in Figure 10d. In the beginning, as shown in Figure 10d, the torque achieves its maximum level of 0.029 p.u., and then the fault emerges at a time point of 0.02 to 0.15 s, and the value drops to 0.01 to 0.003 p.u.

Figure 11 indicates I_s and V_s along the d-axis, stator voltage along the q-axis, and torque at 20% unhealthy circumstances in phase A. Stator current during 20% phase A shorted turns is shown in Figure 11a. Figure 11a reveals that the failure occurs between 0.09 and 0.13 s. In Figure 11b, the voltage across the d-axis of the stator with 20% of the turns shorted during phase A is shown. The issue appears as seen in the figure after the problem has occurred and the V_s has been flowing properly for 0.092 to 0.12 s.

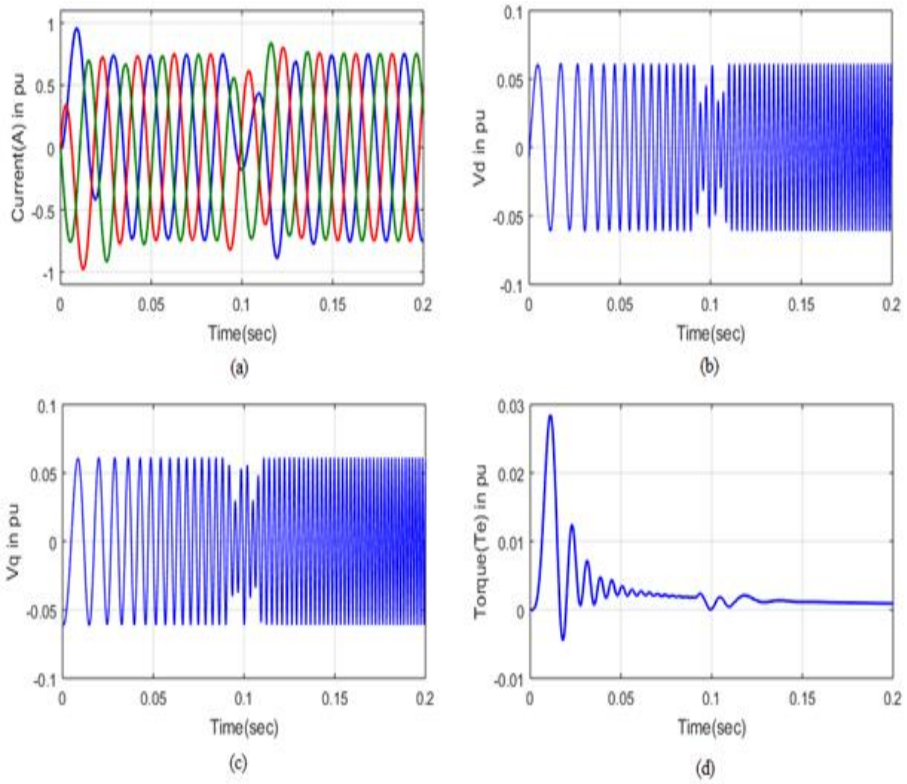

Figure 10. Output Waveforms (**a**) I_s (**b**) V_{sd} (**c**) V_{sq} (**d**) T_s during shorted turns in phase 'A' of 10%.

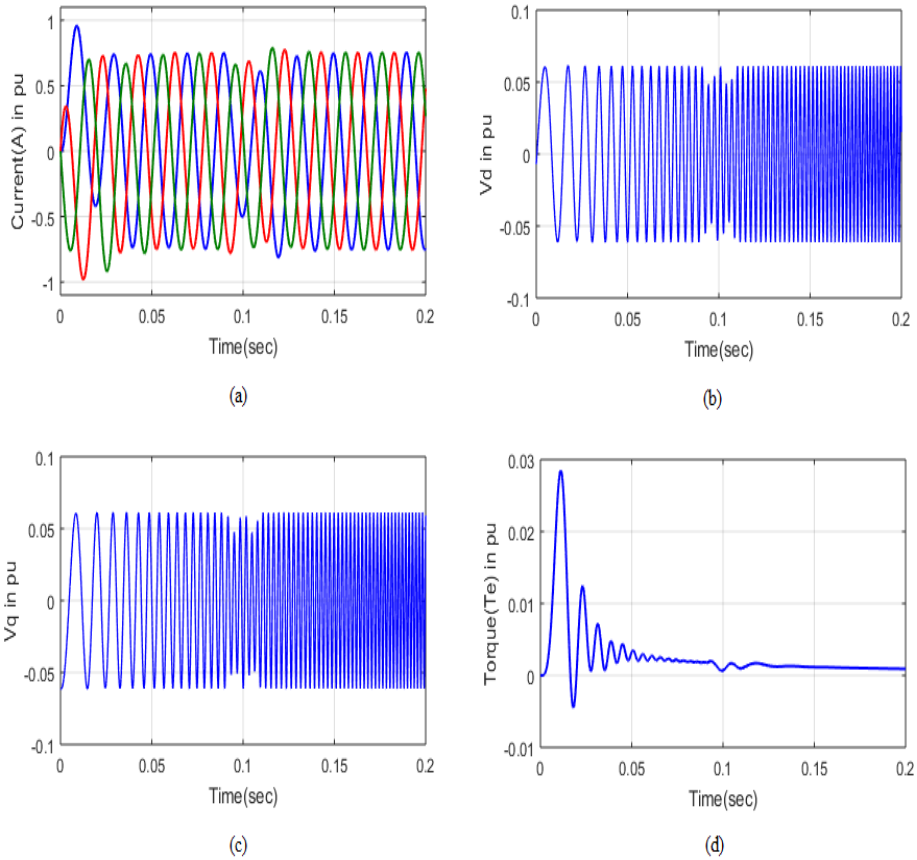

Figure 11. Output Waveforms (**a**) I_s (**b**) V_{sd} (**c**) V_{sq} (**d**) T_s during shorted turns in phase 'A' of 20%.

Figure 11c illustrates the voltage at the q-axis of the stator during 20% shorted rotations in phase A. Primarily, there is no disturbance in the V_s at the q axis, as shown in Figure 11c, but at some point, between t = 0.083 and 0.13 s, a defect appears in the stator voltage at the q axis. Torque at 20% phase A short turns is shown in Figure 11d. Figure 11dshows that at first the torque is at its highest, 0.0295 p.u., but then the fault emerges between 0.02 and 0.15 s, bringing the value down to 0.013 to 0.002 p.u. Figure 12 displays the I_s and V_s at d-axis, V_s at q-axis, and torque output in phase A at 50% load. The current in the stator during 50% phase A shorted turns is shown in Figure 12a. This fault occurs between 0 and 0.05 s in time, as seen in Figure 12a. In Figure 12b, we can see the stator voltage along the d-axis at 50% phase A during shorted turns. The defect in the stator voltage is shown in the figure to manifest between 0.08 and 0.12 s after the fault has occurred, during which time the stator voltage is shown to be flowing properly.

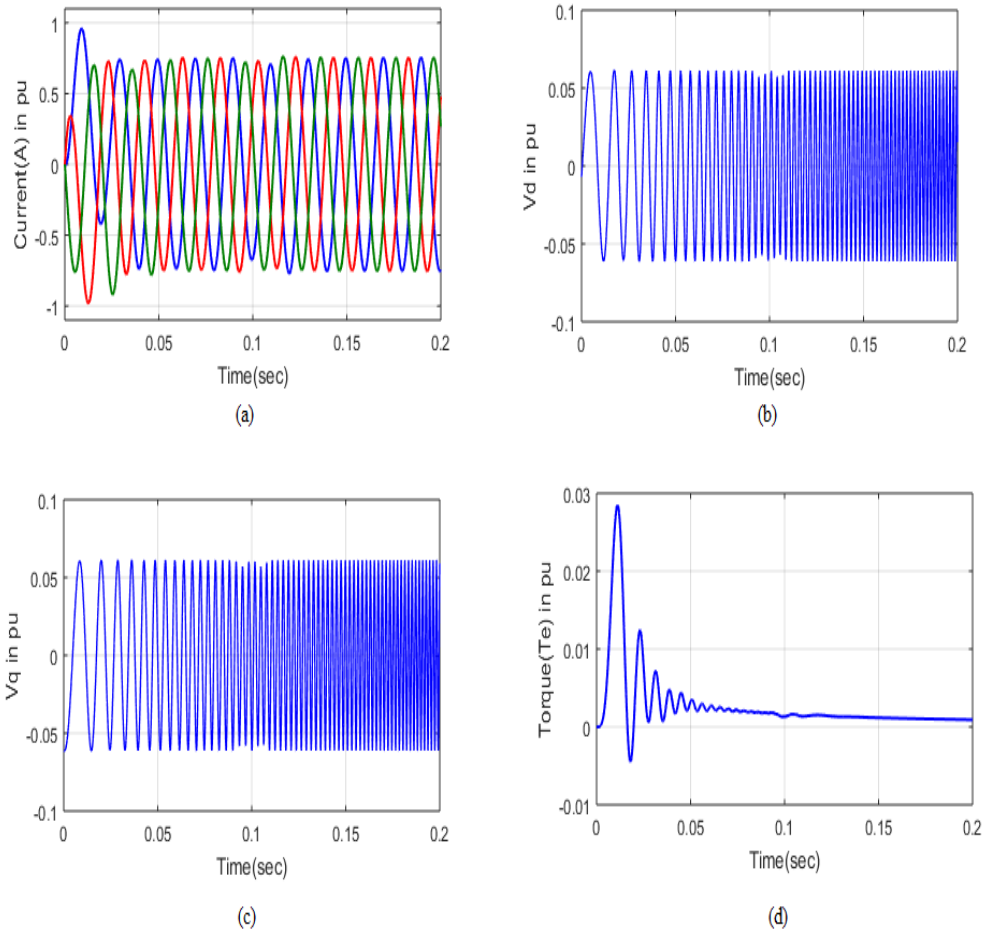

Figure 12. Output Waveforms (**a**) I_s (**b**) V_{sd} (**c**) V_{sq} (**d**) T_s during shorted turns in phase 'A' of 50%.

The q-axis stator voltage during shorted turns at 50% phase A is shown in Figure 12c. Figure 12c shows that there was no initial voltage disturbance along the q axis of the stator, but that a fault developed between t = 0.075 and 0.135 s. The torque at 50% phase A short rotations is shown in Figure 11d. Torque peaks at 0.0298 p.u., as shown in Figure 12d, before dropping to 0.012–0.002 p.u. when the fault emerges at a time of 0.01–0.12 s. In Figure 13, we see the stator current, stator voltage at the d-axis, stator voltage at the q-axis, and torque performance at 10% phase B load under unhealthy conditions. The current through the stator at 10% phase B shorted turns is shown in Figure 13a. Figure 13a reveals that the failure occurs between 0.09 and 0.13 s.

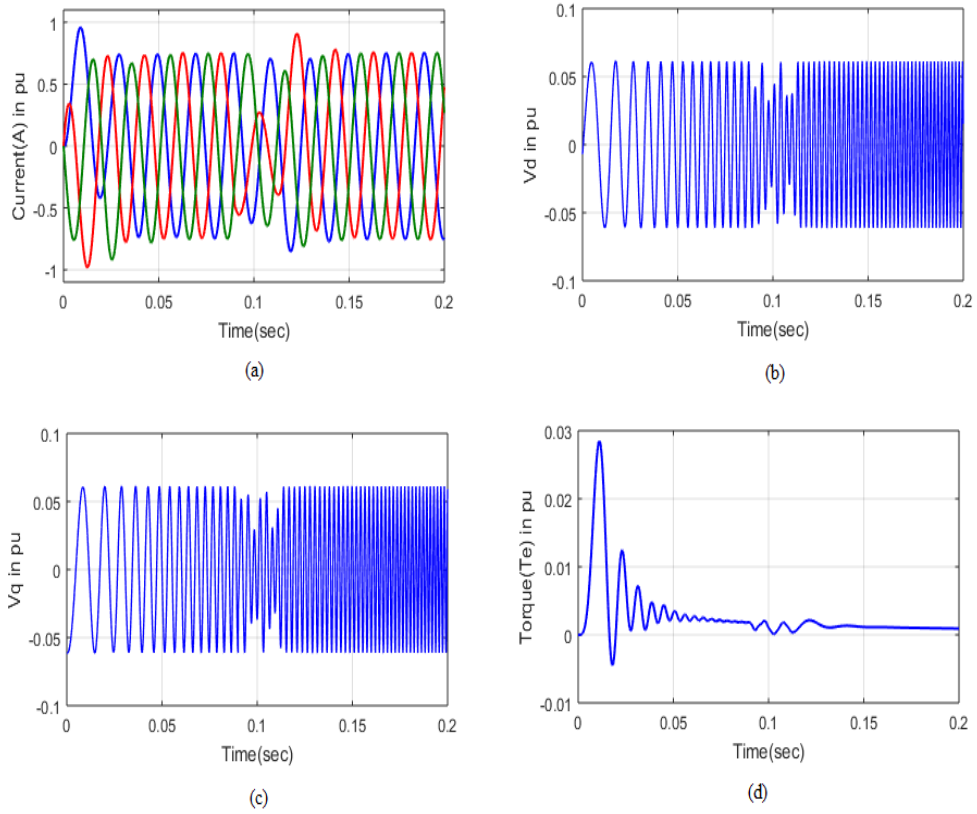

Figure 13. Output Waveforms (**a**) I_s (**b**) V_{sd} (**c**) V_{sq} (**d**) T_s during shorted turns in phase 'B' of 10%.

During 10% phase B shorted turns, the stator voltage is shown in Figure 13b along the d-axis. The defect in the stator voltage is shown in the figure to manifest between 0.08 and 0.11 s after the fault has occurred, during which time the stator voltage is shown to be flowing properly. The q-axis stator voltage during 10% phase B shorted turns is shown in Figure 13c. Figure 13c shows that there is no anomaly in the stator voltage at the q axis at the outset, but that a defect develops between t = 0.09 and 0.135 s into the measurement. Torque for 10% of short turns in phase B is shown in Figure 13d. Initially, the torque achieves its maximum level, shown in Figure 13d, at 0.0299 p.u., and then, between 0.01 and 0.02 s later, the fault emerges, causing the value to drop from 0.03 to 0.14 p.u. The 20% and 50% models' phase B operations are analysed similarly.

Figure 14 illustrates the V_s and I_s at d-axis, Vs at q-axis, and torque at 10% unhealthy circumstances in phase C. The current through the stator during 10% phase C shorted turns is shown in Figure 14a. Figure 14a reveals that the malfunction takes place between 0.09 and 0.13 s in duration. The d-axis stator voltage during 10% shorted turns in phase C is shown in Figure 14b. The defect in the stator voltage is shown in the figure to manifest between 0.08 and 0.12 s after the fault has occurred during periods of normal stator voltage flow. During 10% phase C shorted turns, as shown in Figure 14c, the V_s is measured along the q-axis.

As can be seen in Figure 14c, the stator voltage at the q axis is stable at the outset but develops a fault between t = 0.095 and 0.13 s. The 10% torque for short rotations in phase C is seen in Figure 14d. According to Figure 14d, the torque achieves its maximum value of 0.028 p.u. at a time between 0.01 and 0.02 s, when the fault manifests itself, and subsequently drops to a range of 0.01 to 0.14 p.u. thereafter. Both the 20% and 50% models' phase C operations are analysed. Figure 15 illustrates the behaviour of V_s and I_s at the d-axis, stator voltage at the q-axis, and torque at 10% phase AB under unhealthy circumstances. The 10% shorted turns in phase AB are shown in Figure 15a. Figure 15a demonstrates that the malfunction takes place between 0.08 and 0.14 s.

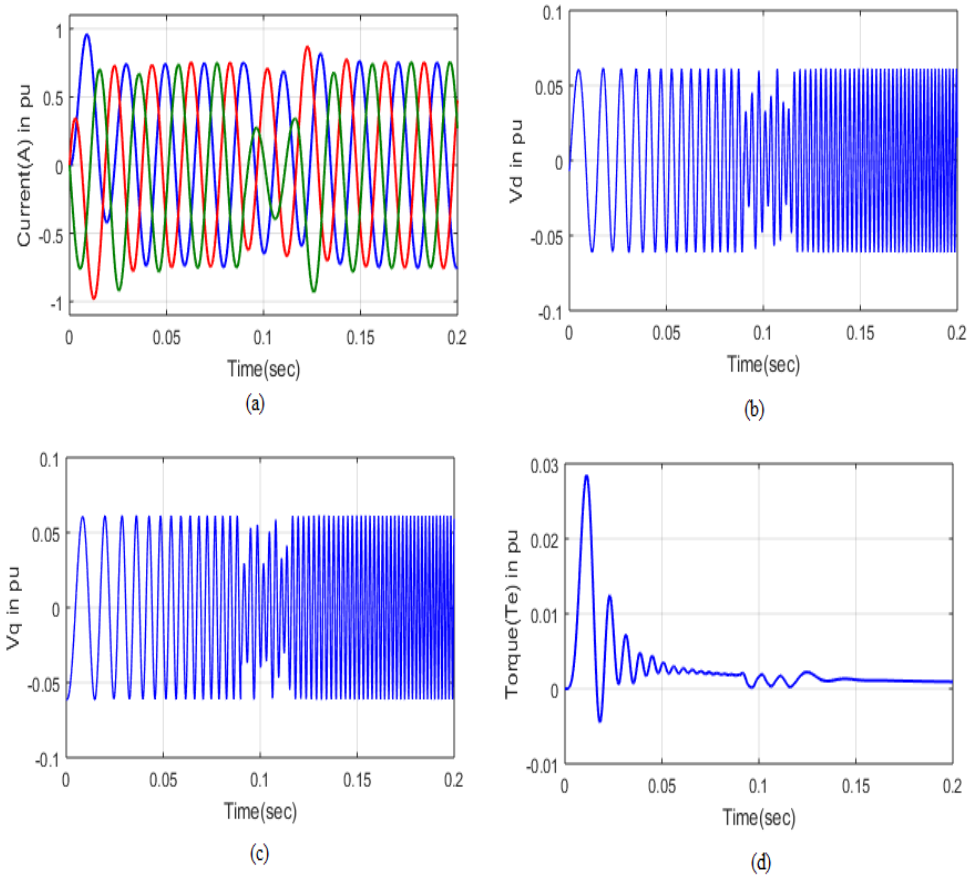

Figure 14. Output Waveforms (**a**) I_s (**b**) V_{sd} (**c**) V_{sq} (**d**) T_s during shorted turns in phase 'C' of 10%.

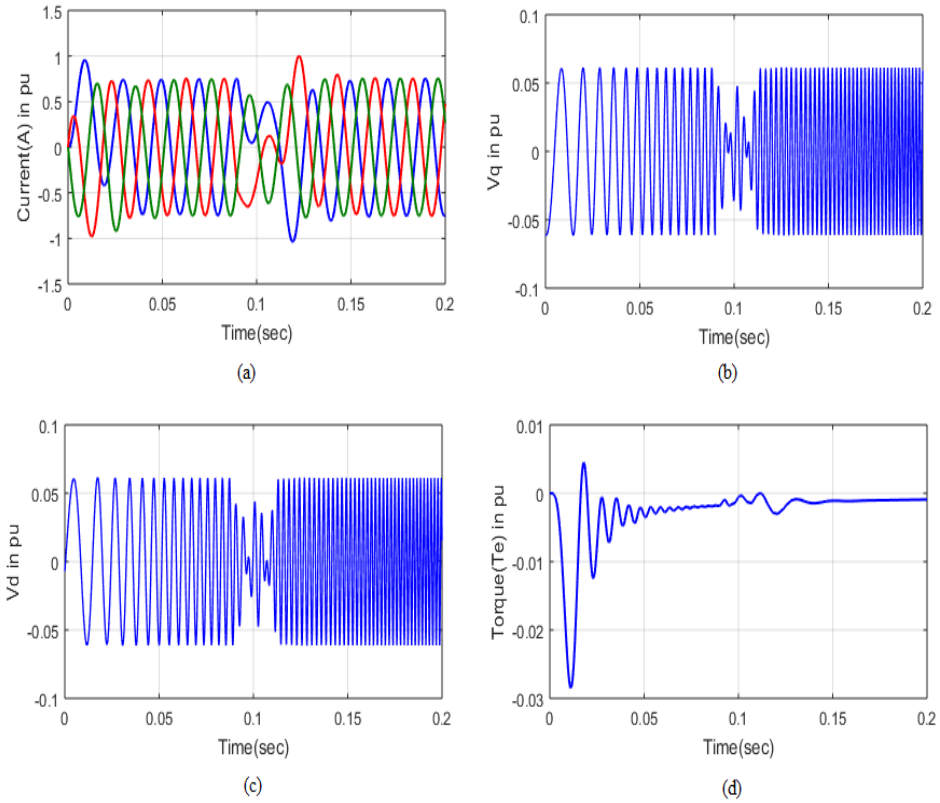

Figure 15. Output Waveforms (**a**) I_s (**b**) V_{sd} (**c**) V_{sq} (**d**) T_s during shorted turns in phase 'AB' of 10%.

During 10% phase AB shorted turns, as seen in Figure 15b, the voltage at the stator's d-axis increases by 5%. The defect in the stator voltage is shown in the figure to manifest between 0.08 and 0.12 s after the fault has occurred during periods of normal stator voltage flow. The q-axis stator voltage is shown in Figure 15c after 10% phase AB shorted rotations. This problem in the stator voltage at the q axis first became apparent between t = 0.08 and 0.12 s, as shown in Figure 15c. During 10% turn shortening in phase AB, as seen in Figure 15d, a torque is applied. The problem arises between 0.005 and 0.02 s into the graph and causes the torque to drop from its highest value of 0.005 p.u. to a lower range of 0.01 to 0.14 p.u. Both the 20% and 50% models' AB-phase functionality is examined.

During unhealthy circumstances in phase BC of 10%, the I_s and V_s at d-axis, stator voltage at q-axis, and torque are all shown in Figure 16. The current through the stator at 10% phase BC shorted turns is shown in Figure 16a. If we look at Figure 16a, we can observe that the malfunction takes place between 0.08 and 0.14 s. The d-axis stator voltage during 10% shorted turns in phase BC is shown in Figure 16b. The problem in the stator voltage is shown in the figure to manifest between 0.085 and 0.115 s after the fault has occurred, whereas the stator voltage was apparently flowing properly beforehand. The q-axis stator voltage during 10% shorted turns in phase BC is shown in Figure 16c. Figure 16c shows that there was no initial voltage disturbance along the q axis of the stator, but that a fault developed between t = 0.08 and 0.115 s. Torque at 10% phase BC short turns is seen in Figure 16d. We can see that the fault arises between 0.01 and 0.02 s after the torque reaches its greatest value (0.005 p.u.) in Figure 16d. Both the 20% and 50% models are analysed for their performance in phase BC. During hazardous circumstances in phase CA of 10%, Figure 17 illustrates the I_s and V_s at d-axis, stator voltage at q-axis, and torque.

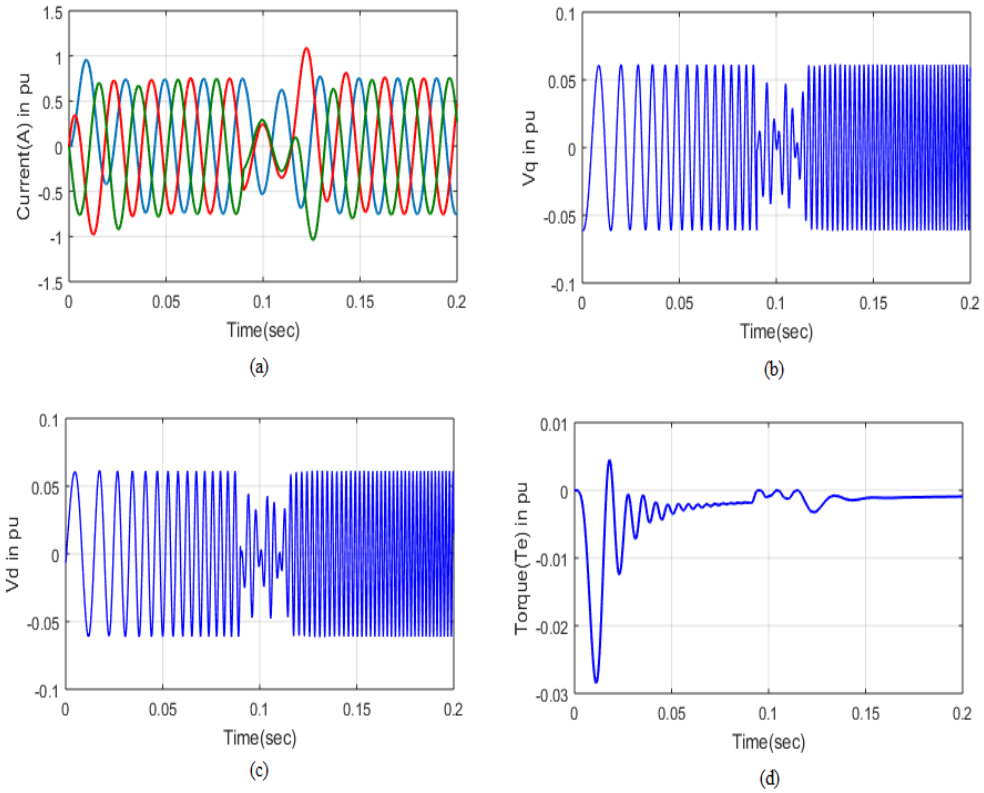

Figure 16. Output Waveforms (**a**) I_s (**b**) V_{sd} (**c**) V_{sq} (**d**) T_s during shorted turns in phase 'BC' of 10%.

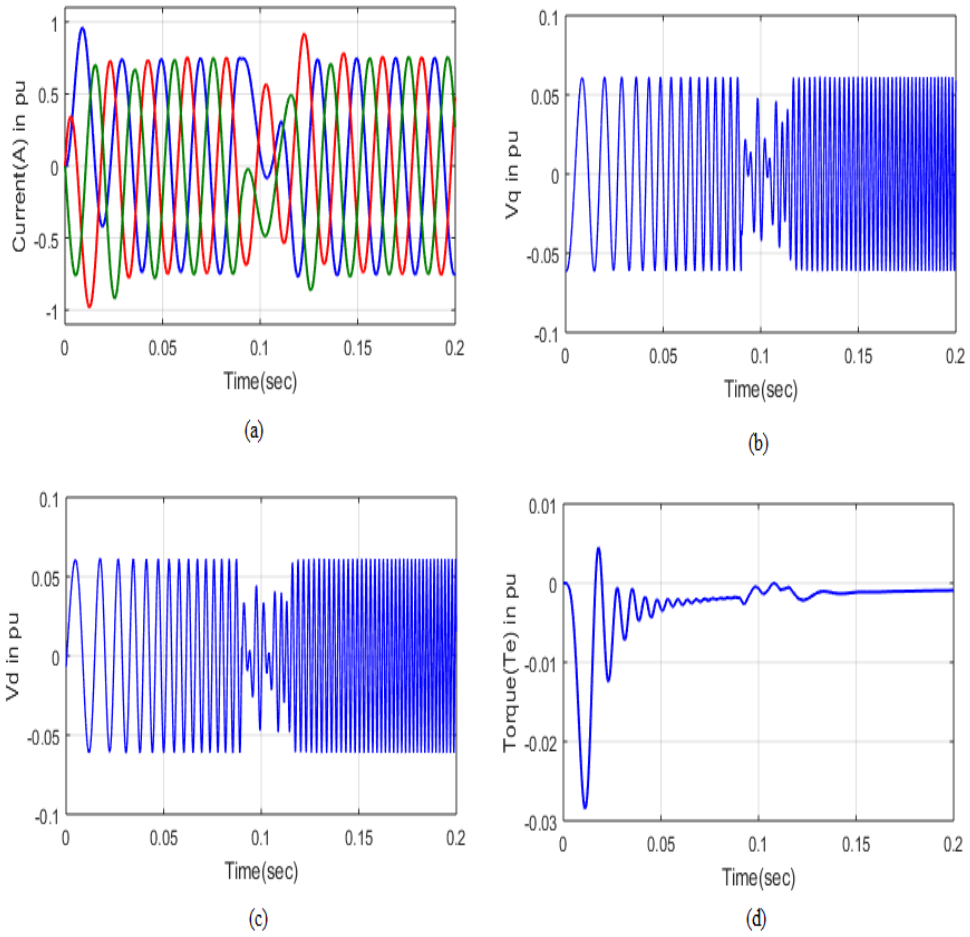

Figure 17. Output Waveforms (**a**) I_s (**b**) V_{sd} (**c**) V_{sq} (**d**) T_s during shorted turns in phase 'CA' of 10%.

In Figure 17a, we can see the stator current at 10% phase CA during shorted revolutions. Figure 17a reveals that the malfunction occurs between 0.08 and 0.14 s. The d-axis stator voltage during 10% phase CA shorted turns is shown in Figure 17b. The problem in the stator voltage is shown in the figure to manifest between 0.085 and 0.115 s after the fault has occurred, whereas the stator voltage was apparently flowing properly beforehand.

The q-axis stator voltage during 10% phase CA shorted turns is shown in Figure 17c. A problem formed in the stator voltage along the q axis between t = 0.08 and 0.115 s, as shown in Figure 17c. Torque at 10% CA phase short turns is seen in Figure 17d. Figure 17d shows that the fault arises between 0.01 and 0.02 s after the torque reaches its maximum value of 0.005 p.u. Similarly, both the 20% and 50% models' phase CA operations are analysed.

Figure 18 represents the I_s, V_s at the d-axis, V_s at the q-axis, and torque at 10% unhealthy phase ABC circumstances. Figure 18a illustrates the I_s at 10% phase ABC shorted turns. Figure 18a reveals that the malfunction takes place between 0.07 and 0.13 s. Voltage at the d-axis of the stator at 10% shorted turns in phase ABC is shown in Figure 18b. The problem in the stator voltage is shown in the figure to manifest between 0.085 and 0.115 s after the fault has occurred, whereas the stator voltage was apparently flowing properly beforehand.

In Figure 18c, we can see the q-axis stator voltage at 10% ABC phase shorted turns. Figure 18c shows that there was no initial voltage disturbance along the q axis of the stator, but that a fault developed between t = 0.07 and 0.12 s. There is a 10% increase in torque for short turns in phase ABC, as seen in Figure 18d. Initially, the torque achieves its maximum value of 0.005 p.u., as shown in Figure 18d, and the fault emerges between 0.01 and 0.02 s later. The 20% and 50% models' ABC phase operations are analysed with the same attention to detail.

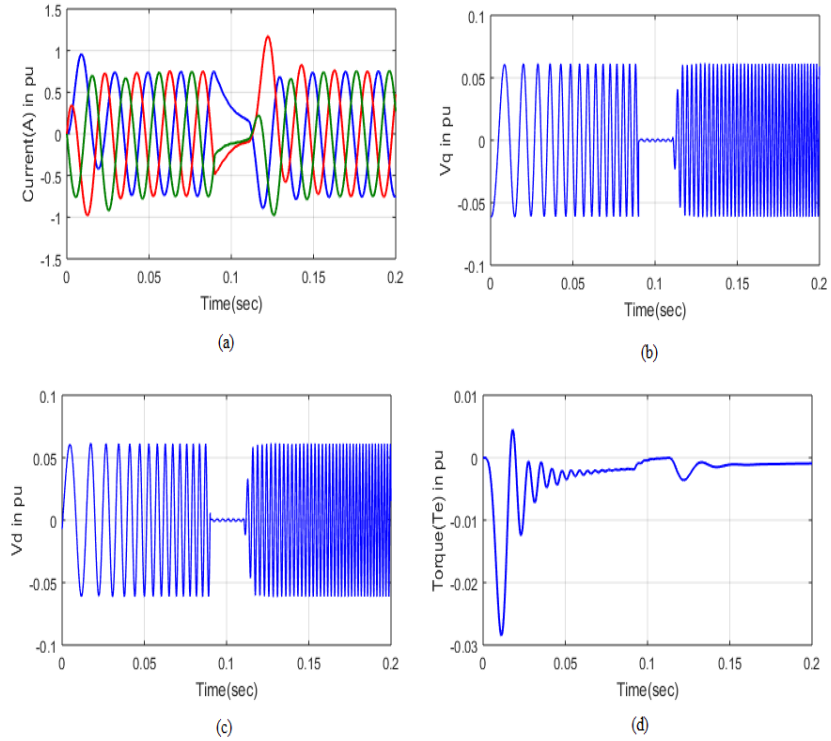

Figure 18. Output Waveforms (**a**) I_s (**b**) V_{sd} (**c**) V_{sq} (**d**) T_s during shorted turns in phase 'ABC' of 10%.

5.3. Performance Analysis

Accuracy, precision, recall, and specificity are some of the metrics of performance covered in this section. All types of interturn defects may be identified and categorised with the help of the suggested method. Existing methods such as ANFIS, RNN, and SSAANN are compared to the suggested strategy's implementation. When 50 and 100 trials have been completed with interturn faults, the performance characteristics of the suggested approach are analysed.

The results of a comparison between the proposed method and the current method for handling an interturn fault are shown in Table 2. Measures of effectiveness, including accuracy, specificity, recall, and precision, for both the current method and the proposed one are listed in Table 2. ANFIS has 0.55% accuracy, 0.50% specificity, 0.60% recall, and 0.52% precision. RNN has 75% specificity, 75% recall, 75% accuracy, 80% precision, and 72% accuracy. SSAANN has a precision of 0.82, a recall of 0.90, a specificity of 0.80, and an accuracy of 0.85. The proposed has a 0.95 accuracy, 0.9 specificity, 0.9% recall, and 0.9% precision. The results of a 100-trial analysis of the suggested method against the status quo during an interturn fault are shown in Table 3. ANFIS has a 0.6 accuracy, 0.53/0.57 specificity, 0.57/0.57 recall, and 0.55/0.55 precision. RNN has a sensitivity of 0.63, specificity of 0.65, recall of 0.60, and precision of 0.65 in its predictions. Accuracy, specificity, recall, and precision are 0.8, 0.75, 0.85, and 0.72with SSAANN. Proposed has a 90% accuracy, 85% specificity, 80% recall, and 95% precision. Tables 2 and 3 show that the suggested approach outperforms conventional methods on a variety of performance metrics. The value of accuracy is calculated using the formula shown in Equation (30).

$$\text{Accuracy} = (TP + TN)/(TP + FP + TN + FN) \quad (30)$$

5.4. Statistical Analysis

Subsequently, we analyse the statistical metrics, including RMS error, maximum absolute percentage error, minimum bias estimation, and average consumption time. The suggested method provides a precise analysis of interturn defects. The suggested method is implemented and then compared to other methods already in use, such as ANFIS,

RNN, and SSAANN. For both 50 and 100 trials with interturn faults, the performance characteristics of the suggested method are analysed. A statistical analysis of the suggested method vs the current method is performed. The RMS error is a measure of the efficiency of the forecasting procedure. The mean-squared deviation indicator is MBE. MAPE is a language of precision indicators.

Table 2. Comparative Analysis for 50 No. of Trials (During ITF).

Performance Measures	ANFIS	RNN	SSAANN	Proposed
Accuracy	0.54	0.76	0.86	0.96
Specificity	0.49	0.69	0.79	0.9
Recall	0.59	0.81	0.91	1
Precision	0.51	0.73	0.83	0.89

Table 3. Comparative Analysis for 100 No. of Trials (During ITF).

Performance Measures	ANFIS	RNN	SSAANN	Proposed
Accuracy	0.61	0.7	0.8	0.9
Specificity	0.54	0.64	0.76	0.84
Recall	0.58	0.59	0.84	0.8
Precision	0.56	0.66	0.71	0.95

The statistical comparison between the suggested method with the established one during an interturn fault is shown in Table 4. ANFIS' RMSE is 26.4, whereas MAPE is 17.2, MBE is 7.1, and TT is 7.8. Consumption time is 6.5 s, MAPE is 6.4%, MBE is 2.9%, and RMSE is 18.9% for RNN. For SSAANN, the RMSE is 23.5, MAPE is 13.0, MBE is 5.1, and consumption time is 8.0. Time to completion (in seconds): 5.2; MAPE: 1; MBE: 2.7; RMSE: 10. In Table 5, we see how the new method stacks up against the established one in the face of an interturn defect throughout a hundred iterations. ANFIS' RMSE is 29, MAPE is 18, MBE is 10.1, and consumption time is 8. For RNN, the RMSE is 21.9%, MAPE is 7.4%, MBE is 5.9%, and consumption time is 7. The RMSE, MAPE, MBE, and consumption time for SSAANN are all 26.5, 14, and 8.3, respectively.

Table 4. Statistic Data Comparison for 50 Number of Trials (During Incipient Fault).

Model	ANFIS	RNN	SSAANN	Proposed
RMSE	26.3	18.8	23.7	10.2
MAPE	17.1	6.3	13	1
MBE	7	2.8	5.2	2.6
Consumption time	7.9	6.5	8.0	5.2

Table 5. Statistic Data Comparison for 100 Number of Trials (During Incipient Fault).

Model	ANFIS	RNN	SSAANN	Proposed
RMSE	29.3	21.8	26.4	13.6
MAPE	18.1	7.5	14.0	2.2
MBE	10.2	5.8	8.2	5.6
Consumption time	8	7	8.3	6

The proposed method has an RMSE of 13.5, MAPE of 2.25, MBE of 5.75, and consumption time of 6. The suggested method's fitness assessment and comparison to the current method are shown in Figure 19. Fitness assessment using the suggested approach is shown in Figure 19a. At 30 iterations, the suggested method reaches convergence. The fitness graph contrasting the suggested method with the conventional one is shown in Figure 19b. Compared to ANFIS's 60 iterations, RNN's 50, and SSAANN's 42, the suggested method successfully converges in 30 iterations.

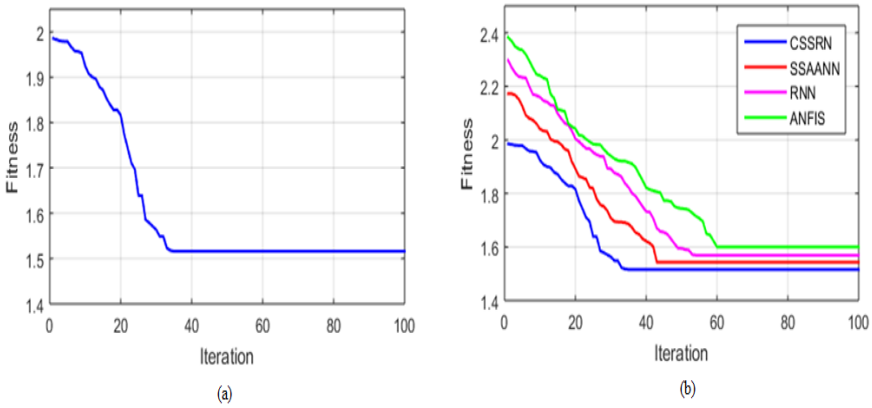

Figure 19. Fitness evaluation (**a**) Proposed system (**b**) Comparative analysis.

6. Conclusions

Using the CSSRN technique, this study examines the interturn insulation flaw in an Asynchronous Motor (AM). The suggested method in this case entails two stages: identification and categorization of the interturn insulation problem in the Asynchronous Motor (AM). The SSA method is used to identify the best practices and produce high-quality data sets. Using the completed dataset, RNNs are able to identify and characterise IM interturn insulation faults in healthy and unhealthy situations. The MATLAB/Simulink platform is used to implement the suggested method for identifying and categorizing fault types. The execution of the suggested approach is validated under various conditions. A number of trials werecarried out and performance metrics such as accuracy, recall, precision, and specificity and statistical measures such as RMSE, MAPE, MBE, and consumption time werecompared to existing techniques such as RNN, ANFIS and SSAANN. The proposed CSSRN approach achieves convergence in 30 iterations, whereas ANFIS needs 60 iterations, RNN needs 50, and SSAANN needs 42. As a future scope of the work, the suggested approach shall be implemented and compared with other modern algorithms such as LSTM networks, variational auto encoders, or convolutional networks.

Author Contributions: Conceptualization, Methodology and Software Validation, G.V.; Formal Analysis, Investigation, Writing review and Editing, A.K.U.; Data curation, Visualisation, A.B.; Methodology and Resources, M.A.H.; Conceptualization, Writing—Original Draft, F.A.; Data Curation, Investigation, R.M.E.; Conceptualization, Methodology and Supervision, K.R.; Methodology and Validation, M.H.A. All authors have read and agreed to the published version of the manuscript.

Funding: This research received no external funding.

Institutional Review Board Statement: Not applicable.

Informed Consent Statement: Not applicable.

Data Availability Statement: Not applicable.

Acknowledgments: This work was supported by the Researchers Supporting Project number (RSPD2023R646), King Saud University, Riyadh, Saudi Arabia. The authors would like to acknowledge Irfan Khan from CARES Laboratory, Texas A&M University, USA and Raghavendra Rajan Vijaya Raghavan from Harman Connected Services India Pvt Ltd., India for the technical expertise provided to finalise this work.

Conflicts of Interest: The authors declare no conflict of interest.

List of Abbreviation and Symbols

List of Symbols and Abbreviations	Terminology
SSO	Salp Swarm Optimization
RNN	Recurrent Neural Network
ANFIS	Adaptive Neuro Fuzzy Inference System
SSAANN	Salp Swarm Algorithm Artificial Neural Network
RMSE	Root mean squared error
MBE	Mean bias error
MAPE	Mean absolute percentage error
ITSC	Interturn Short Circuits
MCSA	Motor Current Signature Analyses
SVD	Singular Value Decomposition
STFT	Short-Time Fourier Transform
r_r	Equivalent Rotor Resistance Per Phase
T_f	Friction Moment
φ_q^{short}	Linkage Flux for the Shorted Turns
MLE	Maximum-Likelihood Estimation
GLRT	Generalised Likelihood Ratio Test
ITIF	Interturn Insulation Fault
SVM	Support Vector Machines
I_q^s, I_d^s, I_o^s	Stator Currents
V_q^s, V_d^s, V_o^s	Stator Voltages
r_s	Stator Resistance Per Phase
z_{ji}	Weight On The Connection From The I^{th} Input Unit
φ_q^r, φ_d^r	Rotor Flux Linkages
ω_b	Base Speed
σ_j^h	Bias For Neuron's Hidden Layer For $j = 1, 2 \cdots h$
P_i	Input 3-Phase Power Supplied To An IM Is Estimated
ξ	Learning Factor

References

1. Nandi, S.; Toliyat, H.A.; Li, X. Condition monitoring and fault diagnosis of electrical motors—A review. *IEEE Trans. Energy Convers.* **2005**, *20*, 719–729. [CrossRef]
2. Haji, M.; Toliyat, H.A. Pattern recognition-a technique for induction machines rotor broken bar detection. *IEEE Trans. Energy Convers.* **2001**, *16*, 312–317. [CrossRef]
3. Seera, M.; Lim, C.P.; Ishak, D.; Singh, H. Fault detection and diagnosis of induction motors using motor current signature analysis and a hybrid FMM–CART model. *IEEE Trans. Neural Netw. Learn. Syst.* **2011**, *23*, 97–108. [CrossRef] [PubMed]
4. Eren, L.; Devaney, M.J. Bearing Damage Detection via Wavelet Packet Decomposition of the Stator Current. *IEEE Trans. Instrum. Meas.* **2004**, *53*, 431–436. [CrossRef]
5. Mirafzal, B.; Demerdash, N.A. On innovative methods of induction motor interturn and broken-bar fault diagnostics. In Proceedings of the IEEE International Conference on Electric Machines and Drives, San Antonio, TX, USA, 15 May 2005. [CrossRef]
6. Karaboga, D.; Kaya, E. Adaptive network based fuzzy inference system (ANFIS) training approaches: A comprehensive survey. *Artif. Intell. Rev.* **2019**, *52*, 2263–2293. [CrossRef]
7. Ballal, M.S.; Khan, Z.J.; Suryawanshi, H.M.; Sonolikar, R.L. Adaptive neural fuzzy inference system for the detection of interturn insulation and bearing wear faults in induction motor. *IEEE Trans. Ind. Electron.* **2007**, *54*, 250–258. [CrossRef]
8. Zidani, F.; Diallo, D.; Benbouzid, M.E.H.; Naït-Saïd, R. A fuzzy-based approach for the diagnosis of fault modes in a voltage-fed PWM inverter induction motor drive. *IEEE Trans. Ind. Electron.* **2008**, *55*, 586–593. [CrossRef]
9. Joksimovic, G.M.; Penman, J. The detection of interturn short circuits in the stator windings of operating motors. *IEEE Trans. Ind. Electron.* **2000**, *47*, 1078–1084. [CrossRef]
10. Gandhi, A.; Corrigan, T.; Parsa, L. Recent advances in modeling and online detection of stator interturn faults in electrical motors. *IEEE Trans. Ind. Electron.* **2010**, *58*, 1564–1575. [CrossRef]
11. Stavrou, A.; Sedding, H.G.; Penman, J. Current monitoring for detecting interturn short circuits in induction motors. *IEEE Trans. Energy Convers.* **2001**, *16*, 32–37. [CrossRef]
12. Yakhni, M.F.; Cauet, S.; Sakout, A.; Assoum, H.; Etien, E.; Rambault, L.; El-Gohary, M. Variable speed induction motors' fault detection based on transient motor current signatures analysis: A review. *Mech. Syst. Signal Process.* **2023**, *184*, 109737. [CrossRef]
13. Rodríguez, P.V.J.; Arkkio, A. Detection of stator winding fault in induction motor using fuzzy logic. *Appl. Soft Comput.* **2008**, *8*, 1112–1120. [CrossRef]

14. Shah, D.; Nandi, S.; Neti, P. Stator-interturn-fault detection of doubly fed induction generators using rotor-current and search-coil-voltage signature analysis. *IEEE Trans. Ind. Appl.* **2009**, *45*, 1831–1842. [CrossRef]
15. De Angelo, C.H.; Bossio, G.R.; Giaccone, S.J.; Valla, M.I.; Solsona, J.A.; García, G.O. Online model-based stator-fault detection and identification in induction motors. *IEEE Trans. Ind. Electron.* **2009**, *56*, 4671–4680. [CrossRef]
16. Önel, I.Y.; Benbouzid, M.E.H. Induction motor bearing failure detection and diagnosis: Park and concordia transform approaches comparative study. *IEEE ASME Trans. Mechatron.* **2008**, *13*, 257–262. [CrossRef]
17. Bakhri, S.; Ertugrul, N. A Negative Sequence Current Phasor Compensation Technique for the Accurate Detection of Stator Shorted Turn Faults in Induction Motors. *Energies* **2022**, *15*, 3100. [CrossRef]
18. Henao, H.; Razik, H.; Capolino, G.A. Analytical approach of the stator current frequency harmonics computation for detection of induction machine rotor faults. *IEEE Trans. Ind. Appl.* **2005**, *41*, 801–807. [CrossRef]
19. Sanchez, O.D.; Martinez-Soltero, G.; Alvarez, J.G.; Alanis, A.Y. Real-Time Neural Classifiers for Sensor and Actuator Faults in Three-Phase Induction Motors. *Machines* **2022**, *10*, 1198. [CrossRef]
20. Laadjal, K.; Bento, F.; Henriques, K.; Cardoso, A.J.M.; Sahraoui, M. A Novel Indicator-Based On-line Diagnostics Technique of InterTurn Short-Circuit Faults in Synchronous Reluctance Machines. *IEEE Trans. Emerg. Sel.* **2023**, 1. [CrossRef]
21. Bouzid, M.B.K.; Champenois, G.; Tnani, S. Reliable stator fault detection based on the induction motor negative sequence current compensation. *Int. J. Electr. Power Energy Syst.* **2018**, *95*, 490–498. [CrossRef]
22. Elbouchikhi, E.; Amirat, Y.; Feld, G.; Benbouzid, M. Generalized likelihood ratio test based approach for stator-fault detection in a PWM inverter-fed induction motor drive. *IEEE Trans. Ind. Electron.* **2018**, *66*, 6343–6353. [CrossRef]
23. Maraaba, L.; Al-Hamouz, Z.; Abido, M. An Efficient Stator InterTurn Fault Diagnosis Tool for Induction Motors. *Energies* **2018**, *11*, 653. [CrossRef]
24. Rebouças Filho, P.P.; Nascimento, N.M.; Sousa, I.R.; Medeiros, C.M.; de Albuquerque, V.H.C. Reliable approach for detection of incipient faults of short-circuits in induction generators using machine learning. *Comput. Electr. Eng.* **2018**, *71*, 440–451. [CrossRef]
25. Surya, G.N.; Khan, Z.J.; Ballal, M.S.; Suryawanshi, H.M. A simplified frequency-domain detection of stator turn fault in squirrel-cage induction motors using an observer coil technique. *IEEE Trans. Ind. Electron.* **2016**, *64*, 1495–1506. [CrossRef]
26. Javed, M.R.; Shabbir, Z.; Asghar, F.; Amjad, W.; Mahmood, F.; Khan, M.O.; Virk, U.S.; Waleed, A.; Haider, Z.M. An Efficient Fault Detection Method for Induction Motors Using Thermal Imaging and Machine Vision. *Sustainability* **2022**, *14*, 9060. [CrossRef]
27. Dorrell, D.G.; Makhoba, K. Detection of interturn stator faults in induction motors using short-term averaging of forward and backward rotating stator current phasors for fast prognostics. *IEEE Trans. Magn.* **2017**, *53*, 1–7. [CrossRef]
28. Mirjalili, S.; Gandomi, A.H.; Mirjalili, S.Z.; Saremi, S.; Faris, H.; Mirjalili, S.M. Salp Swarm Algorithm: A bio-inspired optimizer for engineering design problems. *Adv. Eng. Softw.* **2017**, *114*, 163–191. [CrossRef]
29. Messaoudi, M.; Flah, A.; Alotaibi, A.A.; Althobaiti, A.; Sbita, L.; Ziad El-Bayeh, C. Diagnosis and Fault Detection of Rotor Bars in Squirrel Cage Induction Motors Using Combined Park's Vector and Extended Park's Vector Approaches. *Electronics* **2022**, *11*, 380. [CrossRef]
30. Orosz, T.; Pánek, D.; Rassõlkin, A.; Kuczmann, M. Robust Design Optimization of Electrical Machines and Devices. *Electronics* **2022**, *11*, 1427. [CrossRef]
31. Huang, S.R.; Huang, K.H.; Chao, K.H.; Chiang, W.T. Fault analysis and diagnosis system for induction motors. *Comput. Electr. Eng.* **2016**, *54*, 195–209. [CrossRef]
32. Kerboua, A.; Metatla, A.; Kelaiaia, R.; Batouche, M. Real-time safety monitoring in the induction motor using deep hierarchic long short-term memory. *Int. J. Adv. Manuf. Technol.* **2018**, *99*, 2245–2255. [CrossRef]
33. Kerboua, A.; Metatla, A.; Kelailia, R.; Batouche, M. Fault Diagnosis in Induction Motor using Pattern Recognition and Neural Networks. In Proceedings of the IEEE International Conference on Signal, Image, Vision and Their Applications, Guelma, Algeria, 26–27 November 2018. [CrossRef]
34. Talebi, H.A.; Khorasani, K.; Tafazoli, S. A recurrent neural-network-based sensor and actuator fault detection and isolation for nonlinear systems with application to the satellite's attitude control subsystem. *IEEE Trans. Neural Netw.* **2008**, *20*, 45–60. [CrossRef] [PubMed]
35. Luo, X.; Liao, Y.; Toliyat, H.A.; El-Antably, A.; Lipo, T.A. Multiple coupled circuit modeling of induction machines. *IEEE Trans. Ind. Appl.* **1995**, *31*, 311–318. [CrossRef]